

PIC-MCC Simulations of Capacitive RF Discharges for Plasma Etching

Yoshinori Takao, Kenji Matsuoka, Koji Eriguchi, and Kouichi Ono

*Department of Aeronautics and Astronautics, Graduate School of Engineering, Kyoto University,
Yoshida-Honmachi, Sakyo-ku, Kyoto 606-8501*

Abstract. A numerical study of parallel-plate rf discharges in Ar has been performed including the transport of ions and electrons in the sheath on the substrate. We employ a two-dimensional particle-in-cell with Monte Carlo collisions (PIC/MCC) method for an asymmetric capacitive discharge with an external electrical circuit containing a blocking capacitor and an rf power supply. The model gives self-consistently the dc self-bias voltages that usually occur on the rf-powered electrode, along with the energy and angular distribution of ion and electron fluxes incident on substrate surfaces. The peak electron density obtained in the discharge is $5.0 \times 10^8 \text{ cm}^{-3}$ at the Ar gas pressure of 20 mTorr, rf frequency of 13.56 MHz, and rf voltage of 100 V, where the dc self-bias voltage is determined to be -60 V . For the range of rf voltage (50–400 V) and frequency (13.56–40.68 MHz) examined, the peak electron density increases linearly with rf voltage and frequency squared. Higher rf frequency leads to larger distribution at lower incident angle of ions (more normal to the substrate surface), so that more desirable angular distribution is obtained.

Keywords: PIC, Monte Carlo, Capacitively coupled plasma, Etching, IEDF, IADF

PACS: 52.50.Dg, 52.50.Qt, 52.65.Pp, 52.65.Rr, 52.80.Pi

INTRODUCTION

Controlling features during plasma etching has been a critical problem of interest in the fabrication of modern microelectronic devices. The etched profiles are strongly dependent on the transport of ions and neutrals onto the substrate surfaces through the sheath. The particle transport in microstructures is considerably difficult to be understood, along with the surface reaction processes therein, owing to few methods for diagnostics and to a number of physical and chemical effects that occur [1].

Low temperature capacitively coupled plasma (CCP) discharges are widely used for plasma etching. As feature sizes shrink in the devices, plasma etching applications have transitioned to low pressures to reduce collision induced broadening of the ion angular distribution. Compared with the moderate and high pressure regimes, CCP operation at low pressures remains relatively less well understood as kinetic effects start playing a prominent role in the discharge dynamics [2]. Attention is focused on the effects of rf voltage and frequency on the structure of low pressure plasma discharges, and the energy and angular distribution of ions incident on the substrate.

A numerical model of low pressure CCP in Ar has been developed to analyze the transport of charged particles in the sheath. The simulation employed a two-dimensional particle-in-cell with Monte Carlo collisions (PIC/MCC) method [3, 4], for an asymmetric capacitive discharge with an external electrical circuit containing a blocking capacitor and an rf power supply. Thus, the model gives self-consistently the dc self-bias voltages that occur on the rf-powered electrode and the energy and angular distribution of ion and electron fluxes incident on the substrate surfaces thereon.

NUMERICAL MODEL

Figure 1 shows a schematic of the parallel-plate rf plasma reactor of interest in this study. The reactor consists of a grounded cylindrical chamber 25 cm in diameter and 4 cm in length, with an rf-powered electrode 10 cm in diameter at the bottom of the chamber. Thus, there is a large difference in size between the rf-powered and grounded

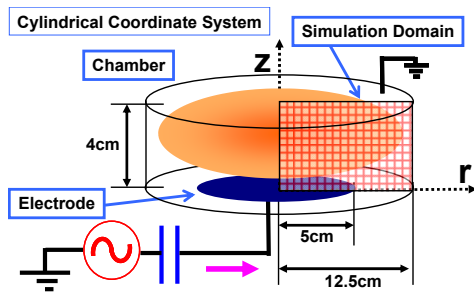


FIGURE 1. Schematic of the parallel-plate rf plasma reactor presently simulated, with the cylindrical coordinate system used in the calculation.

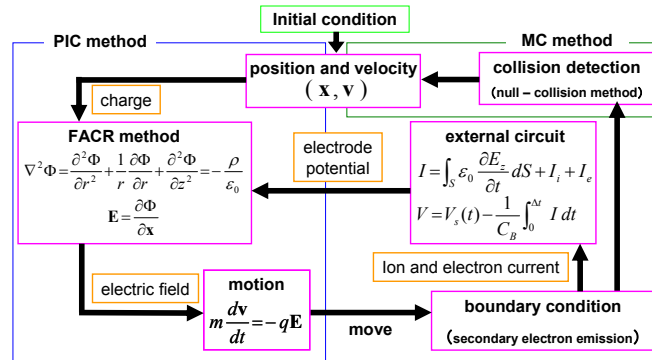


FIGURE 2. Schematic of the flowchart of the plasma simulation. The transport of ions and electrons is simulated with the PIC method and ion-neutral collisions and electron-neutral collisions are simulated with the MC method. The results of external circuit calculations give feedback to the boundary condition of the Poisson equation.

electrodes, i.e., the discharge is asymmetric. The powered electrode is coupled to an rf power supply through a blocking condenser with the capacitance $C_B = 500$ pF, and the working gas is Ar. The time-varying voltage of the rf source is taken as $V_s(t) = V_0 \sin(\omega t)$ with $f = \omega/2\pi = 13.56\text{--}40.68$ MHz.

Figure 2 shows the flowchart of the plasma simulation of interest in this study. The simulation was conducted, assuming the following conditions.

- (i) Only Ar ions and electrons are treated as particles, and the ion species of interest is singly-ionized Ar^+ only.
- (ii) The neutral particles have a Maxwellian velocity distribution at the gas temperature of 300 K ($= 0.026$ eV).
- (iii) The reactions taken into account are elastic scattering, excitation, and ionization for electrons, and elastic scattering and charge exchange for ions, as below.
 - (a) $e + \text{Ar} \rightarrow e + \text{Ar}$ (Elastic Scattering)
 - (b) $e + \text{Ar} \rightarrow e + \text{Ar}^*$ (Excitation)
 - (c) $e + \text{Ar} \rightarrow e + \text{Ar}^+ + e$ (Ionization)
 - (d) $\text{Ar}^+ + \text{Ar} \rightarrow \text{Ar} + \text{Ar}^+$ (Charge Exchange)
 - (e) $\text{Ar}^+ + \text{Ar} \rightarrow \text{Ar}^+ + \text{Ar}$ (Elastic Scattering)
- (iv) The motion of excited-state atoms is not considered.
- (v) Coulomb collisions are not taken into account because of the low plasma density.
- (vi) The coordinate system is axisymmetric, in which a number of simulated particles (or superparticles for ions and electrons) are loaded in a two-dimensional spatial mesh (r, z), along with three velocity components (v_r, v_θ, v_z).

The equation of motion for particles is given by

$$m \frac{d\mathbf{v}}{dt} = -q \frac{\partial \Phi}{\partial \mathbf{r}} \quad (1)$$

where m is the particle mass, $\mathbf{v} = d\mathbf{r}/dt$ the velocity, q the charge, \mathbf{r} the position, and Φ the local electrostatic potential. The numerical time step Δt is taken to be 1.475×10^{-11} s (1/5000 of an rf cycle for 13.56 MHz) for electrons and 3.687×10^{-10} s (1/200 of an rf cycle) for ions, according to their difference in the speed of motion. The ion-neutral and electron-neutral collisions in the gas phase are described by the null-collision method [5]; moreover, secondary electron emission is also included with an emission coefficient $\gamma = 0.75$, through energetic ion bombardment on powered electrode surfaces. The data on the cross sections for electron-neutral and ion-neutral collisions are the same as those used in Refs. [6–12]. The postcollision velocities of electrons and ions are determined by the use of the conservation equations for momentum and energy [3].

The potential in the discharge is derived from the Poisson equation in the cylindrical coordinates:

$$\nabla^2 \Phi = \frac{\partial^2 \Phi}{\partial r^2} + \frac{1}{r} \frac{\partial \Phi}{\partial r} + \frac{\partial^2 \Phi}{\partial z^2} = -\frac{\rho}{\epsilon_0} \quad (2)$$

where ρ is the charge density and ϵ_0 is the permittivity of vacuum. The computational region is divided into equally spaced 100 grids along the r axis and 64 grids along the z axis. The equation is solved by the Fourier-Analysis and Cyclic Reduction (FACR) method with boundary conditions $\Phi = 0$ at the chamber walls and $\Phi = V$ at the rf-

powered electrode, where V is determined by calculating the voltage and current in the external electrical circuit at every time step for ions [13, 14].

The current I in the circuit is calculated from the conservation of charge at the powered electrode:

$$I = I_d + I_c = \int_S \varepsilon_0 \frac{\partial E_z}{\partial t} dA + I_c \quad (3)$$

where I_d is the displacement current, and I_c is the conduction current which consists of the flux of ions I_i and electrons I_e from the plasma onto the electrode surfaces and the flux of secondary electrons from the electrode. Note that $\int_S dA$ denotes the surface integral over the powered electrode surfaces, and the electric field thereat $E_z = -\partial\Phi/\partial z$ is given by the potential Φ obtained from Eq. (2). The electrode potential or voltage V at the new time step is calculated based on the circuit equation:

$$V = V_s(t) - \frac{Q}{C_B} = V_s(t) - \frac{1}{C_B} \int_T I dt \quad (4)$$

where Q denotes the charge stored in the blocking capacitor. Eq. (2) is solved with the V given by Eq. (4) as the boundary condition at the new time step. Thus, we take into account the effects of the external circuit on the potential distribution in the discharge, which in turn gives the dc self-bias voltages self-consistently after the iteration of these calculations until the system reaches a steady state.

RESULTS AND DISCUSSION

Figure 3 shows the two-dimensional distribution of the electron density n_e and the potential Φ averaged over one rf cycle for the gas pressure of 20 mTorr, the rf voltage of 100 V, and the rf frequency of 13.56 MHz, exhibiting significant sheath structures around the rf-powered electrode (at $z = 0$). The peak electron density obtained in the discharge is $5.0 \times 10^8 \text{ cm}^{-3}$, where the plasma potential Φ_p and the dc self-bias voltage V_{dc} is 30 V and -60 V, respectively. The electron density increases with increasing pressure in the range from 20 to 200 mTorr, showing the narrower sheath structure for higher pressures (not shown here). The increase in electron density is due to the increase in neutral gas particles, whereas the ionization degrees decrease.

Figure 4 shows the time-varying behavior of the currents I , I_d , I_i , and I_e at the powered electrode, together with the potentials V thereat and Φ_p in the discharge, which is the average of the positive potentials at $r = 0$ cm, corresponding to the situations of Fig. 3. The incoming flux I_e of plasma electrons onto the powered occurs only around the period when the electrode potential V reaches its peak and the difference $\Phi_p - V$ between the plasma and electrode potentials is minimum; in contrast, the influx I_i of ions remains almost constant throughout the rf cycle. The incoming ion and electron fluxes averaged over one rf cycle are 0.029 mA/cm^2 at $p = 20$ mTorr. The total circuit current I consists mostly of the displacement current I_d at except the period when the electron current I_e occurs, while the conduction current $I_c = I_i + I_e$ of ions and electrons is relatively significant throughout the rf cycle at the higher pressures.

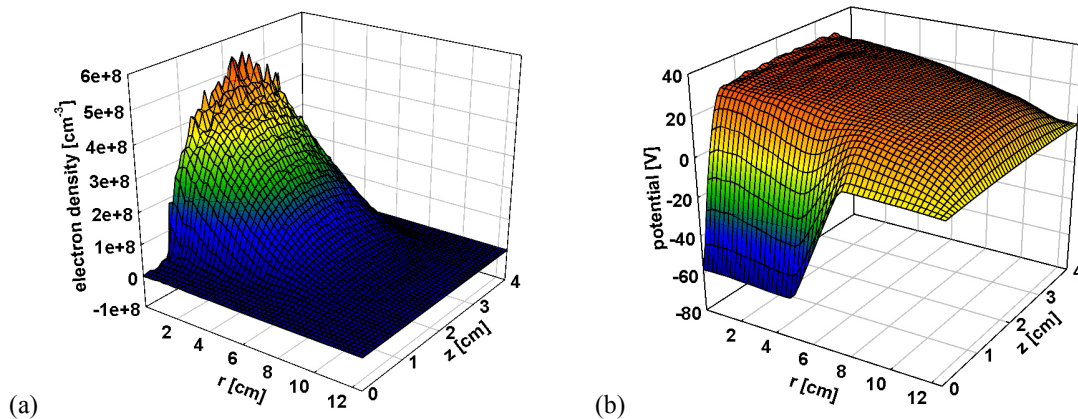


FIGURE 3. Two-dimensional distribution of the (a) electron density n_e and the (b) potential Φ averaged over one rf cycle for the gas pressure of 20 mTorr, the rf voltage of 100 V, and the rf frequency of 13.56 MHz.

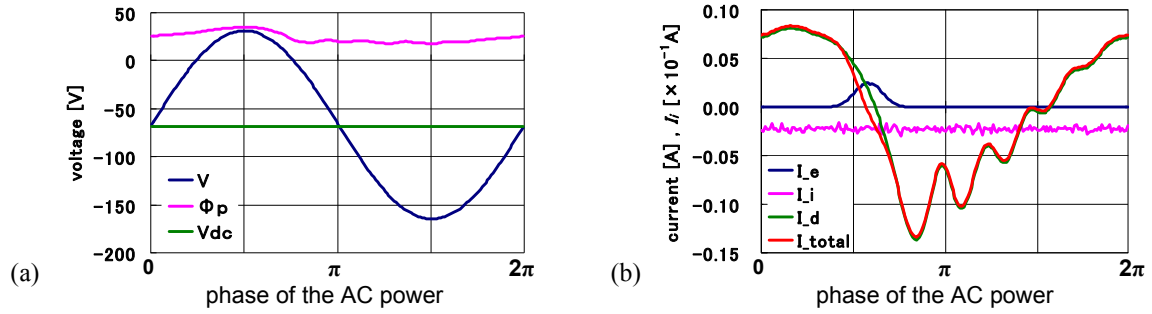


FIGURE 4. (a) Time-varying behavior of the potential V at the rf-powered electrode and the plasma potential Φ_p , which is the average of positive value at $r = 0$ cm, in one rf cycle. (b) Time-varying behavior of the total circuit current I , displacement current I_d , and the flux of ions I_i and electrons I_e at the rf-powered electrode. These correspond to the situation of Fig. 3.

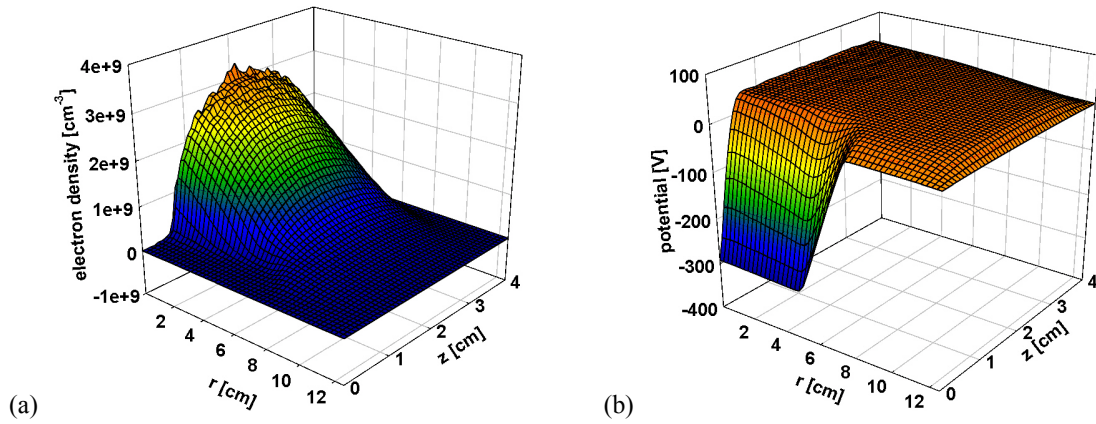


FIGURE 5. Two-dimensional distribution of the (a) electron density n_e and the (b) potential Φ averaged over one rf cycle for the gas pressure of 20 mTorr, the rf voltage of 400 V, and the rf frequency of 13.56 MHz.

Increasing the rf voltage leads to higher electron densities. The peak electron densities obtained at $p = 20$ mTorr and $f = 13.56$ MHz are 1.3×10^9 , 2.0×10^9 , and $3.0 \times 10^9 cm^{-3}$ at the rf voltages of 200, 300, 400 V, respectively. The electron density increases linearly with rf voltage. Figure 5 shows the two-dimensional distribution of the electron density n_e and potential Φ averaged over one rf cycle for the gas pressure of 20 mTorr, the rf voltage of 400 V, and the rf frequency of 13.56 MHz, where the plasma potential Φ_p and the dc self-bias voltage V_{dc} is 30 V and -290 V, respectively. Compared with Fig. 3, wider sheath structure can be seen owing to the larger potential difference between Φ_p and V_{dc} .

Figures 6 shows the energy distribution function of ions (IEDF) and angular distribution function of ions (IADF), incident on the central area ($r < 2.5$ cm) of the rf-powered electrode, averaged over one rf cycle at $p = 20$ mTorr and $f = 13.56$ MHz for rf voltages in the range from 50 to 400 V. As shown in Fig. 6(a), the right side peaks of IEDF are obtained at the ion energy of approximately $\Phi_p + |V_{dc}|$, which can be confirmed from Figs. 3(b), 4(a), and 5(b). For higher rf voltages, bimodal distributions are also exhibited. Since the mean free path of ions is about 0.15 cm at $p = 20$ mTorr ($\lambda_i = 1/330p$ cm, p in Torr [15]) and the sheath widths are determined to be more than 0.5 cm as shown in Figs. 3 and 5, most ions can collide with neutrals through the sheath under the conditions. In our calculation, charge exchange collisions are included. Once an ion accelerated in the sheath undergoes a charge exchange collision, the ion picks up an electron from a slow gas atom and leaves behind a slow scattered ion. The slow ion is scattered isotropically with the temperature of 300 K ($= 0.026$ eV). As ions with slower speed have larger cross sections, lower rf voltages lead to many collisions in the sheath, which can be clearly seen in Fig 6(a). The IADF has a significant peak at around normal incidence (or at an incident angle $\theta \sim 0$ from the electrode surface normal), indicating that a large part of ions impact the electrode almost perpendicularly after being accelerated through the sheath. With increase in rf voltage, larger distributions are obtained at lower incident angles due to less collisions compared with lower rf voltages.

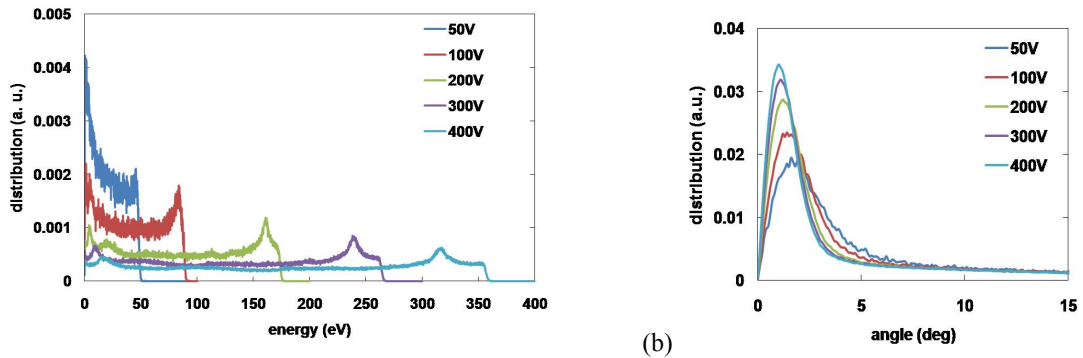


FIGURE 6. (a) Energy distribution function of ions (IEDF) and (b) angular distribution function of ions (IADF) incident on the central area ($r = 2.5$ cm) of the rf-powered electrode averaged over one rf cycle at $p = 20$ mTorr and $f = 13.56$ MHz for rf voltages in the range from 50 to 400 V.

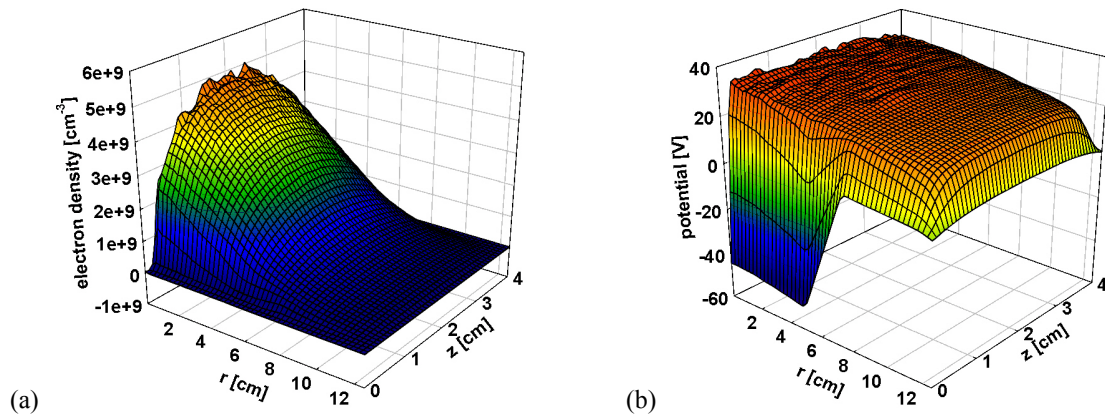


FIGURE 7. Two-dimensional distribution of the (a) electron density n_e and the (b) potential Φ averaged over one rf cycle for the gas pressure of 20 mTorr, the rf voltage of 100 V, and the rf frequency of 40.68 MHz.

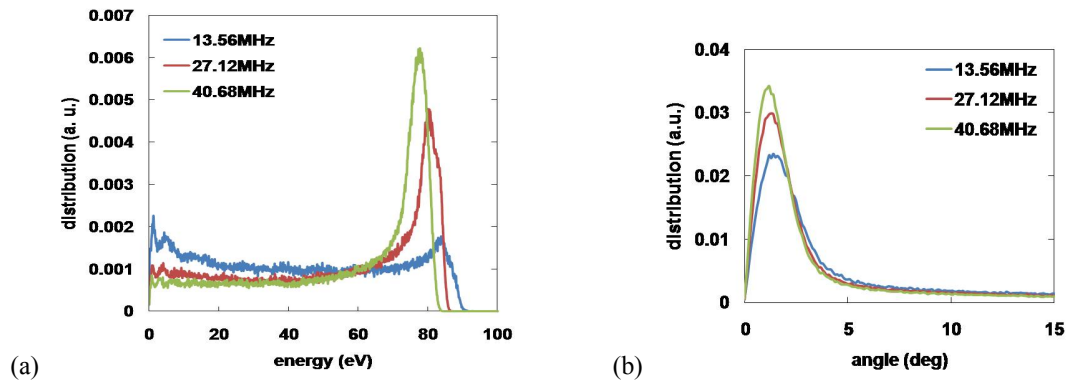


FIGURE 8. (a) Energy distribution function of ions (IEDF) and (b) angular distribution function of ions (IADF) incident on the central area ($r = 2.5$ cm) of the rf-powered electrode averaged over one rf cycle at $p = 20$ mTorr and $V_0 = 100$ V for rf frequencies in the range from 13.56 to 40.68 MHz.

Higher rf frequency results in larger electron density. The peak electron densities obtained at $p = 20$ mTorr and $V_0 = 100$ V are 2.0×10^9 and 5.0×10^9 cm^{-3} at the rf frequencies of 27.12 and 40.68 MHz, respectively. The electron density increases linearly with rf frequency squared. Figure 7 shows the two-dimensional distribution of the electron density n_e and potential Φ averaged over one rf cycle for the gas pressure of 20 mTorr, the rf voltage of 100 V, and the rf frequency of 40.68 MHz. The narrower sheath (< 0.15 cm) can be seen due to the increase in electron density by one order of magnitude compared with Fig. 3(a).

Figure 8 shows the IEDF and IADF incident on the central area ($r < 2.5$ cm) of the rf-powered electrode averaged over one rf cycle at 13.56, 27.12 and 40.68 MHz, respectively, for the gas pressure of 20 mTorr and the rf voltage of 100 V. As shown in Fig. 8(a), higher rf frequencies result in higher IEDF peaks and lower ion energies exhibiting the peaks. Since the rf frequency is more than ten times higher than the ion plasma frequency (a few MHz under the calculation conditions), most ions impinge on the powered electrode with the potential difference between the plasma potential and the dc self-bias voltage, which is about 80 V at 40.68 MHz. Under the condition, the sheath width is comparable to the ion mean free path, so that larger part of ions falls through the sheath to the electrode without collisions in contrast to the case of $f = 13.56$ MHz. Figure 8(b) shows that the IADF has a significant peak at around normal incidence. Increasing rf frequencies leads to larger IADF at lower incident angles, so that more desirable angular distribution is obtained, because the sheath width decreases with increasing rf frequencies and less collisions occur therein.

CONCLUSIONS

Two-dimensional PIC/MCC method for an asymmetric capacitive discharge with an external electric circuit has been employed to investigate the transport of ions and electrons in the sheath of low pressure CCP in Ar. The model gives self-consistently the dc self-bias voltages that usually occur on the rf-powered electrode, along with the energy and angular distribution of ion and electron fluxes incident on substrate surfaces. The peak electron density obtained in the discharge is $5.0 \times 10^8 \text{ cm}^{-3}$ at the Ar gas pressure of 20 mTorr, rf frequency of 13.56 MHz, and rf voltage of 100 V, where the dc self-bias voltage is determined to be -60 V. For the range of rf voltage (50–400 V) and frequency (13.56–40.68 MHz) examined, the peak electron density increases linearly with rf voltage and frequency squared. Since the rf frequency of 40.68 MHz is more than ten times higher than the ion plasma frequency, most ions impinge on the powered electrode with the potential difference between the plasma potential and the dc self-bias voltage. Higher rf frequency leads to larger distribution at lower incident angle of ions (more normal to the substrate surface), so that more desirable angular distribution is obtained.

ACKNOWLEDGMENTS

This work was financially supported in part by a Grant-in-Aid for Scientific Research on Innovative Areas 21110008 from the Ministry of Education, Culture, Sports, Science and Technology.

REFERENCES

1. K. J. Shul and S.L. Pearton, *Handbook of Advanced Plasma Processing Techniques*, Berlin: Springer, 2000.
2. S. Rauf, K. Bera, and K. Collins, *Plasma Sources Sci. Technol.* **19**, 015014 (2010).
3. C. K. Birdsall, *IEEE Trans. Plasma Sci.* **19**, 65 (1991).
4. K. Nanbu, *IEEE Trans. Plasma Sci.* **28**, 971 (2000).
5. V. Vahedi and M. Surendra, *Comput. Phys. Commun.* **87**, 179 (1995).
6. A. Bogaerts, R. Gijbels, and W. Goedheer, *Jpn. J. Appl. Phys.* **38**, 4404 (1999).
7. M. Hayashi, Institute of Plasma Physics, Nagoya University Report No. IPPJ-AM-19, 1981 (unpublished).
8. E. Eggarter, *J. Chem. Phys.* **62**, 833 (1975).
9. L. R. Peterson and J. E. Allen Jr., *J. Chem. Phys.* **56**, 6068 (1972).
10. D. Rapp and P. Englander-Golden, *J. Chem. Phys.* **43**, 1464, (1965).
11. W. H. Cramer, *J. Chem. Phys.* **30**, 641 (1959).
12. M. Surenda, D. B. Graves, and G. M. Jellum, *Phys. Rev. A* **41**, 1112 (1990).
13. J. P. Verboncoeur, M. V. Alves, V. Vahedi, and C. K. Birdsall, *J. Comp. Phys.* **104**, 321 (1993).
14. V. Vahedi and G. DiPeso, *J. Comp. Phys.* **131**, 149 (1997).
15. M. A. Lieberman and A. J. Lichtenberg, *Principles of Plasma Discharges and Materials Processing*, New York: Wiley, 1994, p. 80.